Electric Propulsion Subsystem Optimization for "Ion Beam Shepherd" Missions

F. Cichocki,* M. Merino,† and E. Ahedo‡
Universidad Carlos III de Madrid, 28911 Leganés, Spain
M. Smirnova§ and A. Mingo¶
TransMIT GmbH, 35394 Giessen, Germany
and
M. Dobkevicius**
University of Southampton, Southampton, England SO17 1BJ, United Kingdom

DOI: 10.2514/1.B36105

The ion beam shepherd is an innovative contactless technique for space debris removal in which an impulse transfer thruster pushes the debris object through the action of a plasma plume and an impulse compensation thruster maintains formation flying. The optimal operational point of both thrusters strongly depends on their characteristics and on the physics of the plasma plume expansion into vacuum. With the use of dedicated thruster performance models, complemented with simplified plume expansion and plasma–debris interaction models, a system-level optimization study of the impulse transfer thruster alone and of the overall electric propulsion subsystem is presented for an ion beam shepherd mission example. An optimum design point is found for minimum overall power consumption in both cases.

Nomenclature

d	=	distance between the thruster and the geometrical center of the debris, m
d_0	=	axial extension of the near region of the plasma plume, m
e	=	electron charge, C
F	=	thrust force, N
f_{light}	=	fraction of the orbital period in daylight conditions, %
h	=	self-similarity function in the self-similar plume model
I	=	electric current, A
I_{sp}	=	specific impulse, s
M_0	=	plasma plume initial Mach number
m	=	mass, kg
$\dot{m}$	=	mass flow rate of the electric thruster, kg/s
n	=	plasma plume number density, m^{-3}
P	=	input thruster power, W
q	=	electric charge, C
R_F	=	final radius of the 95% ion current streamtube at the distance of the debris geometrical center, m
R_{TG}	=	radius of the equivalent sphere of the target debris, m
R_{thr}	=	thruster radius, m
R_0	=	initial radius of the 95% ion current streamtube, m
(r, z)	=	radial and axial coordinates in the plasma plume reference frame, m
$\tilde{r}, \tilde{z}$	=	radial and axial coordinates, normalized with R_0
T_e	=	electron temperature, eV
u_r	=	plasma plume radial velocity, m/s
u_z	=	plasma plume axial velocity, m/s
α_F	=	equivalent conical divergence angle of the 95% ion current streamtube at the distance of the debris geometrical center, deg
α_0	=	initial divergence angle of the 95% ion current streamtube, deg
ΔV	=	electric propulsion delta-V, m/s
Δt_{IBS}	=	duration of the shepherding phase, s
$\Delta\phi$	=	electric potential change, assumed positive, V
η_B	=	momentum transfer efficiency of the beam, %
η_m	=	mass utilization efficiency, %
η_T	=	total thrust efficiency, %
ρ	=	specific mass per unit of power, kg/W
ϕ	=	electric potential with respect to the spacecraft ground, V

Subscripts

acc	=	acceleration grid
B	=	plasma beam
chamber	=	inside the discharge chamber
e	=	electrons
eq	=	equivalent from a subsystem point of view
F	=	at the location of the debris geometrical center
IBS	=	ion beam shepherd spacecraft
ICT	=	impulse compensation thruster
ITT	=	impulse transfer thruster
i	=	ions
neut	=	plume neutralization process
PPU	=	power processing units
prop	=	propellant
pwr	=	dedicated power generation subsystem
RF	=	radio-frequency discharge
screen	=	screen grid
TG	=	target space debris object
0	=	at the initial plane or at the origin of the far region plume

Superscript

$*$	=	to be optimized

Received 17 November 2015; revision received 14 June 2016; accepted for publication 27 June 2016; published online 23 August 2016.

*Ph.D. Student, Equipo de Propulsión Espacial y Plasmas; filippo.cichocki@uc3m.es.

†Assistant Professor, Equipo de Propulsión Espacial y Plasmas; mario.merino@uc3m.es.

‡Professor, Equipo de Propulsión Espacial y Plasmas; eduardo.ahedo@uc3m.es.

§Head, IQM; Maria.Smirnova@transmit.de.

¶Project Manager, IQM; aloha.mingo@transmit.de.

**Ph.D. Student; md4g09@soton.ac.uk.

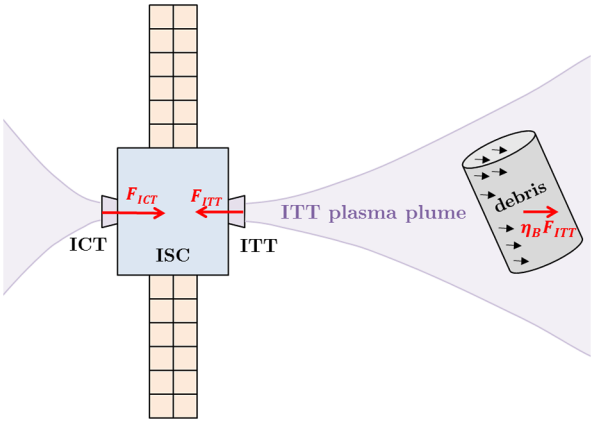

Fig. 1 Schematic of the ion beam shepherd concept.

I. Introduction

THE interest and concern of the scientific community in the space debris problem has been constantly growing in the last decade. The increasing number of space debris objects that populate certain types of orbits (especially the sun-synchronous low Earth orbits and the geostationary orbits) can potentially threaten their exploitation in a relatively close future [1–3], and therefore demands an international effort in two major fields: mitigation strategies and active debris removal/relocation.

First of all, regarding mitigation, it is necessary to define common and international disposal strategies at the end of life of both commercial and scientific satellites. This represents an extra cost to be added to the mission budget (e.g., extra propellant to transfer the satellite from its operative orbit to a disposal orbit), and it ought to be common to all space competitors in the international scene.

Second, efforts have to be put into investigating and demonstrating the technical feasibility of active debris removal (ADR) techniques, which are necessary to effectively stop the growth of the space debris population. In fact, according to a recent study [2], even if all new launches respected the most recent legislation on spacecraft (S/C) postmission disposal strategies (final disposal to a 25 year decay orbit), at least five debris objects per year would need to be actively deorbited in order to prevent the debris number from growing, due to collisions and explosions in the already existing population.

Among many proposed techniques for ADR, the ion beam shepherd (IBS) [4–6] is being considered as a potential candidate by the European Commission, which is currently financing the LEOSWEEP project (which stands for improving low-Earth-orbit security with enhanced electric propulsion [7]), with its major goals being the study of the technical feasibility of the IBS technique and the advance in the design of the related technologies.

The IBS concept is briefly described hereafter. Referring to Fig. 1, an ion beam shepherd S/C makes use of an onboard electric thruster to direct a plasma beam against a target debris. This thruster is called the impulse transfer thruster (ITT) because the impact of the hypersonic ions of its plume produces a net force on the target, which can be deorbited or repositioned "contactlessly" and efficiently to a disposal orbit.

However, because of the thruster plume divergence [8,9], the operating distances are limited to a few times the debris size (with the current plasma propulsion technologies). The effective force transferred to the debris is thus only a fraction of the total ITT thrust F_{ITT}, as shown in Eq. (1), with η_B representing the momentum transfer efficiency of the beam:

$$F_{\mathrm{TG}} = \eta_B F_{\mathrm{ITT}} \tag{1}$$

To maintain formation flying, the ITT has to be compensated by an impulse compensation thruster (ICT), which is located on the opposite side of the IBS. More precisely, formation flying demands that the accelerations on both the IBS and the space debris be equal, meaning that the ICT thrust F_{ICT} is generally higher than that of the ITT [10], as dictated by

$$F_{\mathrm{ICT}} = \left(1 + \eta_B \frac{m_{\mathrm{IBS}}}{m_{\mathrm{TG}}}\right) F_{\mathrm{ITT}} > F_{\mathrm{ITT}} \tag{2}$$

where m_{IBS} and m_{TG} are, respectively, the IBS and target debris masses.

At system level, it is extremely important to identify the operational points of both thrusters (e.g., the operating voltage and the mass flow rate) that yield the lowest possible system mass while complying with a vast set of constraints, ranging from overall power availability to the size and cost of the required components. Such optimal points strongly depend on the distance between the IBS and the debris object, on the thruster types and characteristics, and on the mission specifications. This paper's main goal is to propose an approach for the optimization of the ITT alone and of the overall electric propulsion subsystem (EPS), considering a realistic IBS mission scenario. A preliminary version of this work was already presented at the 34th International Electric Propulsion Conference [11].

Before proceeding with the description of the optimization study, the mission specifications and the IBS power constraints and assumptions are described in Sec. II. The ITT and ICT performance models are introduced in Sec. III. Then, the simplified models for the plasma plume expansion and interaction with the space debris are presented in Sec. IV. The independent optimization of the ITT is described and discussed in Sec. V. Section VI then presents the results of the overall propulsion subsystem optimization, including both the ITT and ICT. Finally, the conclusions of the study are reported in Sec. VII.

II. Mission Specifications and Propulsion Subsystem Constraints

An IBS mission generally consists of two phases: a rendezvous phase with the target debris object, out of the scope of this study; and a shepherding phase, in which the orbit change is carried out with the use of electric propulsion. The specifications of a realistic deorbiting IBS mission are summarized in Table 1. A deorbiting maneuver of approximately 300 km in 170 days or, equivalently, a deorbit rate of approximately 2 km/day has been considered as the baseline mission goal. The debris object weighs 1.5 metric tons and currently orbits in a nearly polar low Earth orbit. Considering an average 67% orbit daylight fraction (thrusters cannot operate on battery power alone due to a S/C design choice), the previously defined specifications on the debris mass and orbit decay rate are equivalent to constraining the transmitted force to the debris F_{TG} to 30 mN. Moreover, the operational distance between the ITT exhaust plane and the debris object must not be lower than 7 m. This threshold corresponds to the half-span of the S/C solar array and has been chosen due to collision safety considerations in the case of a failure of the relative attitude control. Finally, the IBS wet mass m_{IBS} is expected to be around 500 kg.

The electric propulsion subsystem, which is in charge of transmitting the required force to the target, must comply with stringent power constraints at the platform level. Referring to Table 2, the total input power to the power processing units (PPUs) of the EPS is limited to 3 kW. This means that, assuming a PPU energy

Table 1 Deorbiting mission specifications and assumptions

Mission requirements and assumptions	Values	Units
IBS spacecraft mass m_{IBS}	500	kg
Target debris mass m_{TG}	≃1.5	tons
Target debris characteristic diameter	2.5	m
Orbit altitude change	300	km
Orbit altitude change per day	∼2	km/day
Daylight fraction in orbit f_{light}	67	%
Shepherding phase duration Δt_{IBS}	170	days
Achieved target delta-V	0.190	km/s
Required force on the debris F_{TG}	30	mN
Operational distance d between ITT and target debris	≥7	m

Table 2 IBS power constraints and assumptions

EPS constraints and assumptions	Values	Units
Input power to the EPS PPUs	≤3	kW
PPUs efficiency η_{PPU}	85	%
Input power to both thrusters	≤2.6	kW
Specific mass of the power generation subsystem ρ_{pwr}	13.3	kg/kW

conversion efficiency of 85% (a conservative value), this power limit corresponds to 2.6 kW at thruster level. Finally, regarding the power generation subsystem, a value of 13.3 kg/kW is considered for the specific mass of the dedicated solar arrays. This value is representative of the current available technology.

III. Characterization of the ITT and ICT

In this study, both the ITT and the ICT are assumed to be radio-frequency ion thrusters (RIT). This is a particular type of gridded ion thruster, in which the ionization process is achieved through the inductively coupled radio-frequency (RF) antenna, wrapped around the thruster chamber, as shown in Fig. 2. The generated ions are accelerated through a grid system to a kinetic energy given by $q_i \Delta\phi_B$, with q_i representing the ion charge and $\Delta\phi_B$ the effective acceleration beam voltage. As shown in Fig. 2, this beam voltage is the effect of various contributions: the plasma voltage drop within the chamber (a few tens of volts) $\Delta\phi_{\mathrm{chamber}}$, the voltage drop between the screen and acceleration grids (several kilovolts), and a final voltage increment $\Delta\phi_{\mathrm{neut}}$ that brings the potential to a value slightly higher than the potential of the neutralizing hollow cathode [12] (a few tens of volts) and that is necessary to attract the neutralizing electrons. Since the hollow cathode is grounded, the effective beam acceleration voltage is well approximated by the screen grid potential:

$$\Delta\phi_B = \Delta\phi_{\mathrm{chamber}} + (\phi_{\mathrm{screen}} - \phi_{\mathrm{acc}}) - \Delta\phi_{\mathrm{neut}} \simeq \phi_{\mathrm{screen}} \tag{3}$$

For this optimization study, a thruster performance model is needed to explore the behavior of various thruster figures of merit as a function of some design parameters. The details and the justification of such a performance model can be found in [13]. Hereafter, only a summary of the main characteristics of the model is provided. Referring to Fig. 3, the required input variables (or design parameters) are the beam voltage $\Delta\phi_B$ and the thrust force F. The model then provides as output the thruster plume divergence angle α_0, the necessary beam current I_B, the thruster radius R_{thr}, the mass utilization efficiency η_m, and the RF input power P_{RF} necessary to sustain the discharge.

These performance figures follow the dependencies shown in Eqs. (4–8):

$$\alpha_0 \propto \Delta\phi_B^{-\beta_1} \tag{4}$$

$$I_B \propto F\Delta\phi_B^{-1/2} \tag{5}$$

$$R_{\mathrm{thr}} \propto I_B^{1/2} \tag{6}$$

$$\eta_m \propto \ln(R_{\mathrm{thr}}) \tag{7}$$

$$P_{\mathrm{RF}} \propto R_{\mathrm{thr}}^{\beta_2} \tag{8}$$

First of all, the thruster divergence angle α_0 is modeled as a decreasing power law of the beam voltage, with a coefficient $\beta_1 > 1$, as shown in Eq. (4). The beam current is then proportional to the ratio

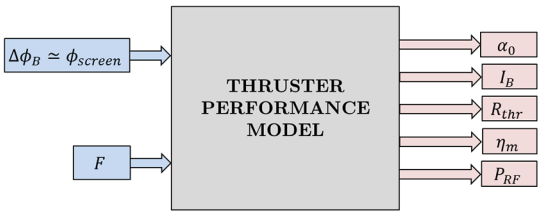

Fig. 3 Block diagram of the performance model used for both the ITT and the ICT.

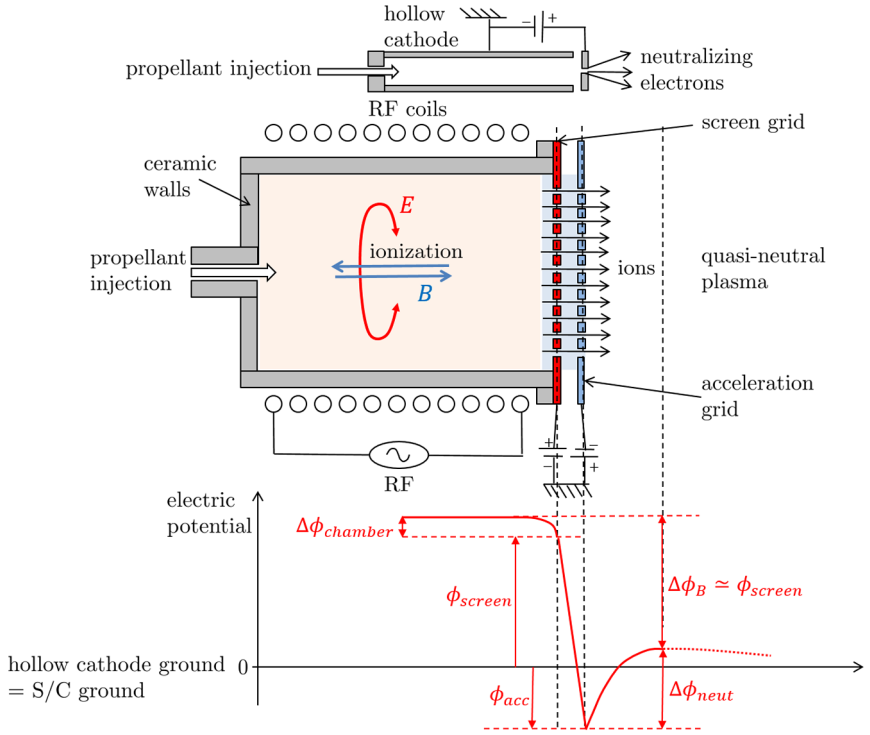

Fig. 2 Generic working principle of a RIT thruster and electric potential evolution across the thruster symmetry axis. Voltage drops and lengths are not to scale.

between the thrust and the ion exhaust velocity (which scales as $\Delta\phi_B^{1/2}$), as shown in Eq. (5). Since the required ion extraction area is proportional to the beam current and grows with the square of the thruster radius, R_{thr} is proportional to the square root of I_B, as dictated by Eq. (6). The mass utilization efficiency η_m increases logarithmically with the thruster radius according to Eq. (7), as a larger thruster requires a lower neutral gas pressure to sustain the RF discharge, and hence features a lower neutral outflow fraction. The required RF input power is also modeled as a function of the thruster radius, and more precisely as a power law with coefficient $\beta_2 > 1$, so that a larger thruster requires a higher RF input power [Eq. (8)].

With the performance figures computed previously, it is then straightforward to obtain the beam power P_B, and hence the total thruster input power, $P = P_B + P_{\text{RF}}$, the mass flow rate $\dot{m}$, the specific impulse I_{sp}, and the total thrust efficiency η_T following their classical definitions, provided in Eqs. (9–13):

$$P_B = I_B \Delta\phi_B \tag{9}$$

$$P = P_{\text{RF}} + P_B \tag{10}$$

$$\dot{m} = \frac{m_i}{q_i}\frac{I_B}{\eta_m} \tag{11}$$

$$I_{\text{sp}} = \frac{F}{\dot{m} g_0} \tag{12}$$

$$\eta_T = \frac{F I_{\text{sp}}}{2P} \tag{13}$$

The models for the ITT and for the ICT only differ in terms of the proportionality constants and power law coefficients in Eqs. (4–8), as discussed in [13].

IV. Modeling the Momentum Transfer Efficiency

A. Simplified Plume Expansion and Debris Interaction Models

A detailed description of the physical phenomena taking place in a plasma plume expansion into vacuum is provided in [8,9]. In summary, the plasma plume generated by a plasma thruster can be divided into two regions, as sketched in Fig. 4. The first region is a near region extending up to a few thruster radii from the thruster exit where collisions, thruster electromagnetic fields, and neutralizer three-dimensional effects dominate the expansion, and where the ion beamlets coalesce into a single-peaked beam. The second region is a far region plume, where these effects become negligible and the smooth single-peaked profile continues to expand under the influence of the residual electron pressure and ambipolar electric field. The complex near-region plume cannot be easily modeled in terms of simple equations, and it is usually characterized experimentally. The far-region plume, on the other hand, can be studied with simplified fluid models, like those in [8,9].

Referring to Fig. 4, we begin by defining a reference frame based on an initial plane located within the far region, at a distance d_0 from the thruster exit. Existing experimental observations of gridded ion thrusters and Hall effect thrusters show that the plume has already become smooth and single-peaked beyond one or two thruster radii from the thruster exit [14–16]. Such a smooth profile is assumed by the self-similar models (SSM), used here to characterize the far plume. Although a direct comparison between these fluid models and the experimental plume data in the very far region is hard to obtain, recent studies [17,18] have shown a good agreement between them, at relatively small distances from the thruster (less than 1 m).

Following the self-similar solution method, first introduced by Parks and Katz [19], at this initial plane, the plume is assumed to have a Gaussian density profile, a constant axial velocity, and a linearly increasing radial velocity. Moreover, the streamtube containing 95% of the ion current has a radius R_0 and a half-cone angle given by the thruster divergence angle α_0, as shown in Fig. 4.

Given the impossibility to obtain experimental near-region data at this design stage of the project, we shall further assume that our far region starts at the exit plane of the thruster (i.e., we take $d_0 = 0$), where the ITT performance model provides the corresponding plume divergence angle α_0. To cover for the potential divergence increase in the near region, a +10% margin on this initial divergence angle (or thruster divergence angle) is included in the following analyses.

The SSM method then allows us to compute the plasma density and velocity through a self-similar expansion function h, which obeys Eq. (14) and can be obtained through numerical integration with the initial condition $h(0) = 1$. In this differential equation, $\tilde{z} = z/R_0$ is the normalized axial coordinate and M_0 is the initial ion Mach number, for which the square represents the ratio between the ion kinetic energy and the electron thermal energy, as shown in Eq. (15), where m_i and q_i are the ion mass and charge (we assume singly charged xenon ions) and T_{e0} is the electron temperature at the origin O of the reference frame of Fig. 4, expressed in energy units (equal to the product of the Boltzmann's constant and the classical temperature):

$$\frac{\mathrm{d}h}{\mathrm{d}\tilde{z}} = \sqrt{\tan^2\alpha_0 + 12\frac{\ln h}{M_0^2}}; \qquad h(0) = 1 \tag{14}$$

$$M_0 = \sqrt{\frac{m_i u_{i0}^2}{T_{e0}}} = \sqrt{\frac{2 q_i \Delta\phi_B}{T_{e0}}} \tag{15}$$

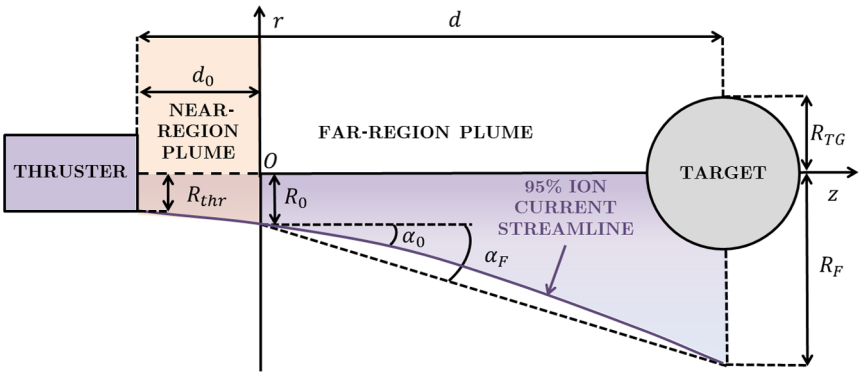

Fig. 4 Sketch of the plasma plume's near and far regions, the plasma streamtube containing 95% of the ion current, and the target debris.

Table 3 Parameters affecting the plume expansion and target interaction

Plume and debris interaction parameters	Values	Units
Electron temperature T_{e0} at the origin O	3.0	eV
Equivalent spherical radius R_{TG} of the debris	1.25	m
Near region axial length d_0	0.0	m
Distance between thruster exit and debris center d	7.0	m
Margin on α_0 to account for near-region effects	10.0	%
Ions mass m_i (xenon)	$2.18 \cdot 10^{-25}$	kg
Ions charge q_i	$1.6 \cdot 10^{-19}$	C

The 95% ion current streamtube radius $R(z)$, the axial and radial plume velocities [$u_z(r, z)$ and $u_r(r, z)$], and the plume density $n(r, z)$ are finally obtained with Eqs. (16–19). Here, n_0 and u_{i0} represent the plasma density and ion velocity at the origin O:

$$R(z) = R_0 h(\tilde{z}) \tag{16}$$

$$u_z(r, z) = u_{i0} \tag{17}$$

$$u_r(r, z) = u_{i0} \frac{\mathrm{d}h}{\mathrm{d}\tilde{z}}(\tilde{z}) \frac{r}{R(z)} \tag{18}$$

$$n(r, z) = \frac{n_0}{h^2(\tilde{z})} \exp\left(-3 \frac{r^2}{R^2(z)}\right) \tag{19}$$

It is worth mentioning that the self-similar solution of Eqs. (14) and (16–19) is valid only for isothermal electrons. Other thermodynamic models for the electrons can be easily employed, such as polytropic electrons; however, the isothermal limit is conservative, in the sense that it causes the largest increase of plume divergence, hence in the context of an IBS mission, the lowest momentum transfer efficiency [8,9]. The electron temperature appearing in Eq. (14) (through M_0) assumes values around 2–3 eV [14,15] in Hall effect thrusters and between 1 and 3 eV in ion thrusters [16]. Therefore, we have assumed the conservative value of $T_{e0} = 3$ eV, as shown in Table 3. In fact, the higher the electron temperature and thermal energy, the higher the increase of divergence in the plume. On the contrary, if we progressively decrease the electron temperature to zero, we get the limit of $M_0 \to \infty$, for which the self-similar function can be easily solved as $h(\tilde{z}) = 1 + \tilde{z} \tan \alpha_0$, corresponding to a perfectly conical plume expansion.

With the plume solution of Eqs. (14) and (16–19), and following the approach of [10], a simplified formula for the fraction of plume momentum intercepted by the debris can be obtained. First, to simplify the analysis, the debris is modeled as an equivalent sphere of radius $R_{\mathrm{TG}} = 1.25$ m (half of the characteristic diameter of the target debris, given in Table 1) and its center is located at a distance d from the thruster exit plane. At this distance, assumed equal to 7 m (the minimum operational distance of Table 1), the radius of the plasma tube carrying 95% of the ion current is R_F, which allows us to define an equivalent conical divergence angle at the debris α_F as

$$\alpha_F = \arctan\left(\frac{R_F - R_0}{d}\right) > \alpha_0 \tag{20}$$

Note that α_F is not the local slope angle of the 95% ion current streamline, as clearly shown in Fig. 4. Integrating the plasma momentum over the surface of the sphere, we can finally compute the momentum transfer efficiency as

$$\eta_B = 1 - \exp\left(-\frac{3 \cdot R_{\mathrm{TG}}^2}{R_F^2 - (\tan \alpha_F \cdot R_{\mathrm{TG}})^2}\right) \tag{21}$$

The assumptions described so far for the characterization of the momentum transfer efficiency are finally summarized in Table 3.

B. Equivalent Conical Divergence Angle at the Debris and Momentum Transfer Efficiency

In this section, the effect of the ITT beam voltage on α_F and η_B is assessed and discussed. With the use of the plume model described in Sec. IV.A, and with the parameters of Table 3, we can obtain a two-dimensional (2-D) map of the equivalent conical divergence angle and of the momentum transfer efficiency as a function of $\Delta\phi_B$ and α_0 for two different values of R_0 (7 and 25 cm), for which the range should include the design radius of the ITT.

Referring to Fig. 5a, as the beam voltage $\Delta\phi_B$ or the initial divergence angle α_0 increases, the difference between the near and equivalent conical divergence angles becomes smaller. Asymptotically, α_F tends to α_0 for both increasing beam voltage and the near-region divergence angle. Regarding the initial plume radius effect, the higher plume radius yields a lower equivalent divergence angle at the debris because the radial electron pressure gradients at the initial plume plane are lower, thus yielding a lower divergence increase.

Figure 5b shows the corresponding dependence of the momentum transfer efficiency on $\Delta\phi_B$ and α_0 for the two initial radius cases. The momentum transfer efficiency increases substantially for decreasing divergence angles and, for a given α_0, it shows a weak dependence on the beam voltage, except at very a low voltage and small initial divergence angle. The effect of the initial plume radius, on the other hand, is twofold. At a sufficiently high beam voltage or divergence angle, when the electron pressure effects are negligible, a higher initial plume radius R_0 automatically yields a higher radius R_F at the target debris, and hence a lower momentum transfer efficiency [through Eq. (21)]. At small initial divergence angles and beam voltages, on the other hand, the increase in divergence angle plays a more important role than the initial plume radius, so that a lower initial radius also yields a lower momentum transfer efficiency.

In our ITT performance model, the near-region divergence angle α_0 is a direct function of the beam voltage, as given by Eq. (4), so that the momentum transfer efficiency (and the equivalent conical divergence angle at the debris) is indeed a function of $\Delta\phi_B$ and R_0.

To evaluate the real effect of the initial plume radius R_0 on the momentum transfer efficiency for our ITT, η_B has been evaluated again for the two different initial radius cases (7 and 25 cm). The use of the thruster performance model of Sec. III has been limited to Eq. (4) to model the dependence of the initial divergence angle on $\Delta\phi_B$ [Eq. (6) has not been considered here]. The momentum transfer efficiency

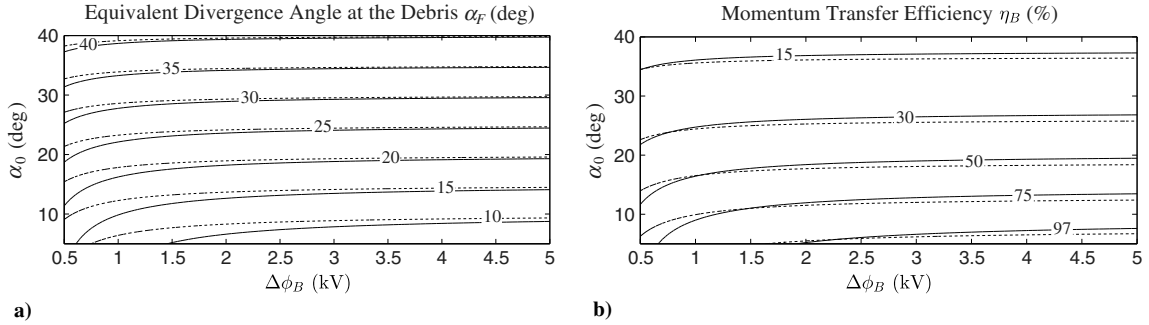

a) b)

Fig. 5 Representations of a) equivalent conical divergence angle and b) momentum transfer efficiency, for $R_0 = 7$ cm (solid line) and 25 cm (dashed line).

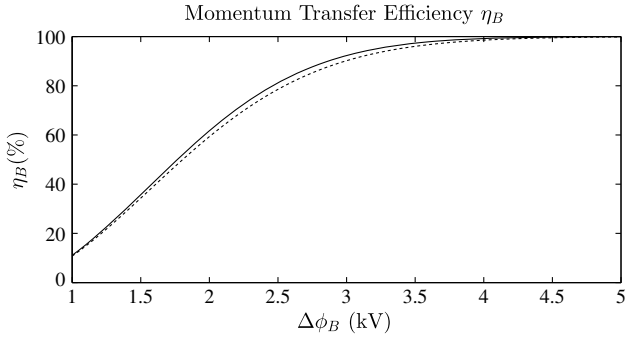

Fig. 6 Momentum transfer efficiency versus $\Delta\phi_B$, for $R_0 = 7$ cm (solid line) and 25 cm (dashed line).

evolution with $\Delta\phi_B$ is shown in Fig. 6. At low beam voltages (below 2.5 kV), the momentum transfer efficiency increases almost linearly with $\Delta\phi_B$, whereas at higher voltages (above 2.5 kV), the increase becomes weaker, saturating at almost 100% for voltages above 4.5 kV.

Although the differences between the two R_0 cases are small (always lower than 5%), the worst-case scenario is clearly represented by the higher initial radius case (25 cm). The 25 cm case is then considered to model conservatively the dependence of η_B on $\Delta\phi_B$ in the optimization study described in the following sections.

Before proceeding with it, however, it is worth further discussing the plume expansion effects on the momentum transfer efficiency. Referring to Fig. 5a, it is apparent that the more hypersonic (the higher M_0 or $\Delta\phi_B$) and the more divergent (the higher α_0) the plume is, the closer to conical its expansion. This conical-like expansion is the major source of momentum transfer efficiency loss, as shown in Fig. 5b, where the iso-η_B lines are almost horizontal and showing a weak dependence on the beam voltage. Under a purely "geometrical" expansion, the plume density decreases with the square of its streamline radius, which is proportional to both the operational distance and $\tan(\alpha_0)$. Therefore, it is paramount to minimize α_0, which generally requires operating at a high beam voltage (Fig. 6).

Second, even if the initial divergence angle is small, the residual electron pressure makes the plume expand further, meaning that the slope of the ion streamlines increases away from the thruster [8,9]. This effect is small in our case, except at very low $\Delta\phi_B$ and α_0 (where the iso-α_F and iso-η_B lines of Figs. 5a and 5b deviate from horizontal lines), and can always be mitigated by increasing the operating Mach number M_0 provided by Eq. (15). For a fixed propellant atom mass, this can be achieved by either increasing the beam voltage $\Delta\phi_B$ or reducing the residual electron temperature T_{e0} in the plume.

V. Optimization of the ITT

Before proceeding with the optimization of the overall EPS, it is useful to first optimize the ITT independently. This means to identify the operating beam voltage of the ITT that maximizes some specific figure of merit. As explained in [13], a key figure of merit for the ITT is the ratio between transmitted force to the debris and input power to the thruster. Referring to Fig. 6, if we operate at a constant ITT thrust, the transferred thrust to the debris grows linearly with $\Delta\phi_B$ at low beam voltages (Fig. 6), whereas the required input power grows with $\Delta\phi_B^{1/2}$ [Eqs. (9) and (5) with F constant]. The transferred thrust-to-power ratio thus increases with $\Delta\phi_B$ until the momentum transfer efficiency begins to saturate and its increase is equal to the increase in input power. The voltage corresponding to this maximum transferred thrust-to-power ratio represents the optimal ITT operational condition.

A method to maximize the previously defined figure of merit is described hereafter. By fixing the transmitted force on the target to the required 30 mN value (see Table 1), we shall look for the operational voltage that minimizes the required ITT input power. First, we compute the required ITT thrust as a function of $\Delta\phi_B$, with the conservative curve of Fig. 6 to express the momentum transfer efficiency:

$$F_{\mathrm{ITT}}(\Delta\phi_B) = \frac{30\ \mathrm{mN}}{\eta_B(\Delta\phi_B)} \tag{22}$$

Then, once $\Delta\phi_B$ and F_{ITT} are fixed, with the use of the performance model of Sec. III, all the thruster performance figures can be obtained, including the input thruster power P_{ITT}. This power is finally plotted in Fig. 7 as a function of $\Delta\phi_B$. As expected, a minimum operating power is found at a $\Delta\phi_B = 3.3$ kV (black dot in the figure), with a corresponding thrust force of 31.9 mN and a momentum transfer efficiency of 94.1%.

The choice of the design voltage of the ITT, however, cannot be determined solely by the maximization of the transferred force to power ratio. A key figure of merit of the ITT is, in fact, the mass utilization efficiency η_m, which should be high. In fact, a low η_m can cause a high number of charge-exchange collisions between ions and neutral atoms in the near region, and hence a large ion backflow towards sensitive S/C surfaces, which could potentially endanger the mission or increase the initial plume divergence α_0 beyond the values assumed here.

At the optimal ITT point discussed previously, the mass utilization efficiency turns out to be 72.2% (according to the ITT performance model). Although it is out of the scope of this paper to assess the effects of such efficiency, it is a key aspect to model when designing a real mission.

Finally, in order to get an idea of how an already existing technology would perform as an ITT, we have chosen the *NASA Solar Technology Application Readiness* (NSTAR) thruster [16,20,21] as a representative candidate. At its throttle level N.9 (out of 15), this thruster features a total input power of 1.57 kW, a beam voltage of 1.1 kV, a thrust force of 62.5 mN, and a 95% ion current divergence angle of 28.5 deg.

Assuming an initial plume radius of 15 cm (equal to the NSTAR thruster radius) and a 10% margin on the initial divergence angle, the NSTAR would feature a momentum transfer efficiency equal to 20.1%, with a transmitted force on the target equal to 12.5 mN. This means that, at a power level close to the minimum of Fig. 7, the NSTAR thruster would achieve the mission in approximately 400 days (versus the 170 days requirement). This illustrates clearly the central importance of a low plume divergence to increase the IBS efficiency and reduce the debris removal time.

VI. Optimization of the Whole Electric Propulsion Subsystem

A. Major Assumptions

The optimization described in Sec. V provides very valuable inputs for the choice of the operational point of the ITT alone. Nevertheless, from an overall subsystem perspective, what needs to be minimized are the input power to the two thrusters P^* and the fraction of the EPS dedicated mass that can be optimized m^*. In this section, we shall describe the approach we have followed to define the optimal operational points (or beam voltages) of the two thrusters that minimize P^* and m^*.

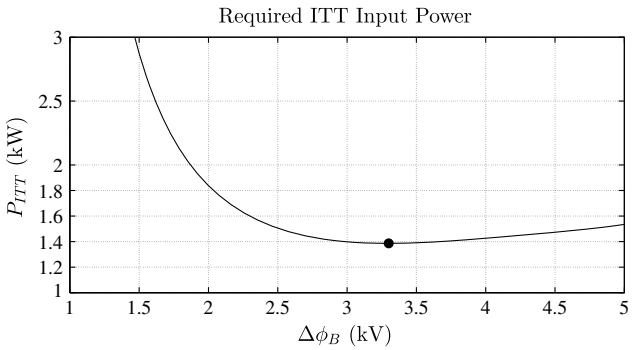

Fig. 7 ITT input power required to transfer a force of 30 mN to the debris.

The total thruster input power to be optimized P^* is simply given by

$$P^* = P_{\mathrm{ITT}} + P_{\mathrm{ICT}} \tag{23}$$

whereas the definition of m^* is less straightforward. The total EPS dedicated mass can be split into several contributions: the two thrusters' mass, $m_{\mathrm{ITT}} + m_{\mathrm{ICT}}$; the total dedicated power generation subsystem mass m_{pwr} (solar arrays' fraction dedicated to the generation of the PPUs input power); the total propellant mass m_{prop}; and the power processing units' mass m_{PPU}. In this study, however, we have considered for m^* only a part of the previously defined EPS dedicated mass, as shown in Eq. (24):

$$m^* = m_{\mathrm{pwr}} + m_{\mathrm{prop}} \tag{24}$$

In fact, the mass contributions of the thrusters and of the PPUs have not been included, as their variations with the operational beam voltage are expected to be quite small. The former (thruster units masses) would slightly depend on the operating conditions, as a higher voltage yields a lower mass flow rate, and hence a smaller and lighter thruster [13]. However, a thruster unit weighs only a few kilograms (at these power levels); hence, its mass variation can be neglected with respect to the major mass contributions: m_{pwr} and m_{prop}. Regarding the PPUs, on the other hand, their mass can hardly be modeled as a linear function of $\Delta\phi_B$ and their mass variation is expected to be small (in the considered range of beam voltages). The remaining mass contributions are modeled as given by Eqs. (25) and (26):

$$m_{\mathrm{prop}} = f_{\mathrm{light}} \Delta t_{\mathrm{IBS}} (\dot{m}_{\mathrm{ITT}} + \dot{m}_{\mathrm{ICT}}) \tag{25}$$

$$m_{\mathrm{pwr}} = \frac{\rho_{\mathrm{pwr}} P^*}{\eta_{\mathrm{PPU}}} \tag{26}$$

where f_{light} and Δt_{IBS} are, respectively, the orbital period fraction in daylight conditions and the shepherding phase duration; $\dot{m}_{\mathrm{ITT}}$ and $\dot{m}_{\mathrm{ICT}}$ are the mass flow rates of the ITT and ICT; and ρ_{pwr} and η_{PPU} are, respectively, the solar array specific mass and the PPU energy conversion efficiency.

The values of all the parameters required by the EPS optimization study are listed in Tables 1 and 2.

B. Overall Optimization Method

The electric propulsion subsystem optimization consists of studying the evolution of figures of merit such as the total thruster input power P^*, the optimizable EPS mass m^*, the total required propellant mass m_{prop}, and the equivalent shepherding delta-V ΔV_{eq} as 2-D functions of $\Delta\phi_{B,\mathrm{ITT}}$ and $\Delta\phi_{B,\mathrm{ICT}}$. For any ITT beam voltage $\Delta\phi_{B,\mathrm{ITT}}$, the following applies:

1) The ITT parameters are computed following the approach of Sec. V with the model of [13] (described in Sec. III).

2) Given the ITT thrust F_{ITT}, the required ICT thrust is obtained through Eq. (2).

3) For a varying ICT beam voltage in a range between 0.5 and 5 kV, the following parameters are computed:
a) The ICT performance figures, with the model of [13] (described in Sec. III); b) the overall (ITT + ICT) thruster input power, $P^* = P_{\mathrm{ICT}} + P_{\mathrm{ITT}}$; c) the overall required propellant mass m_{prop} using Eq. (25); d) the overall power subsystem dedicated mass m_{pwr} using Eq. (26); and e) the equivalent shepherding phase delta-V ΔV_{eq}. An equivalent propulsion subsystem specific impulse is first obtained as follows:

$$I_{\mathrm{sp,eq}} = \frac{\dot{m}_{\mathrm{ITT}} I_{\mathrm{sp,ITT}} + \dot{m}_{\mathrm{ICT}} I_{\mathrm{sp,ICT}}}{\dot{m}_{\mathrm{ITT}} + \dot{m}_{\mathrm{ICT}}} \tag{27}$$

where $I_{\mathrm{sp,ITT}}$ and $I_{\mathrm{sp,ICT}}$ are, respectively, the ITT and ICT specific impulses. Then, through Tsiolkovsky's equation, ΔV_{eq} is computed as

$$\Delta V_{\mathrm{eq}} = I_{\mathrm{sp,eq}} g_0 \ln\left(\frac{m_{\mathrm{IBS}}}{m_{\mathrm{IBS}} - m_{\mathrm{prop}}}\right) \tag{28}$$

where g_0 is the standard gravity acceleration constant.

C. Overall Optimization Results

Following the procedure described in the previous paragraph, the 2-D contours of Fig. 8 have been obtained. Figure 8a shows the total thruster input power P^*. For a given ITT voltage, the total power presents a minimum at an ICT voltage of approximately 1000 V. Then, it starts to increase again because, for a given ICT thrust, the required ICT power grows with the ICT specific impulse (or beam voltage). The lowest total power is 2.54 kW, achieved at the ITT–ICT voltage point (3.58, 1.01) kV. At this point, $F_{\mathrm{ITT}} = 31.1$ mN and $F_{\mathrm{ICT}} = 40.6$ mN. It is important to underline that small changes in

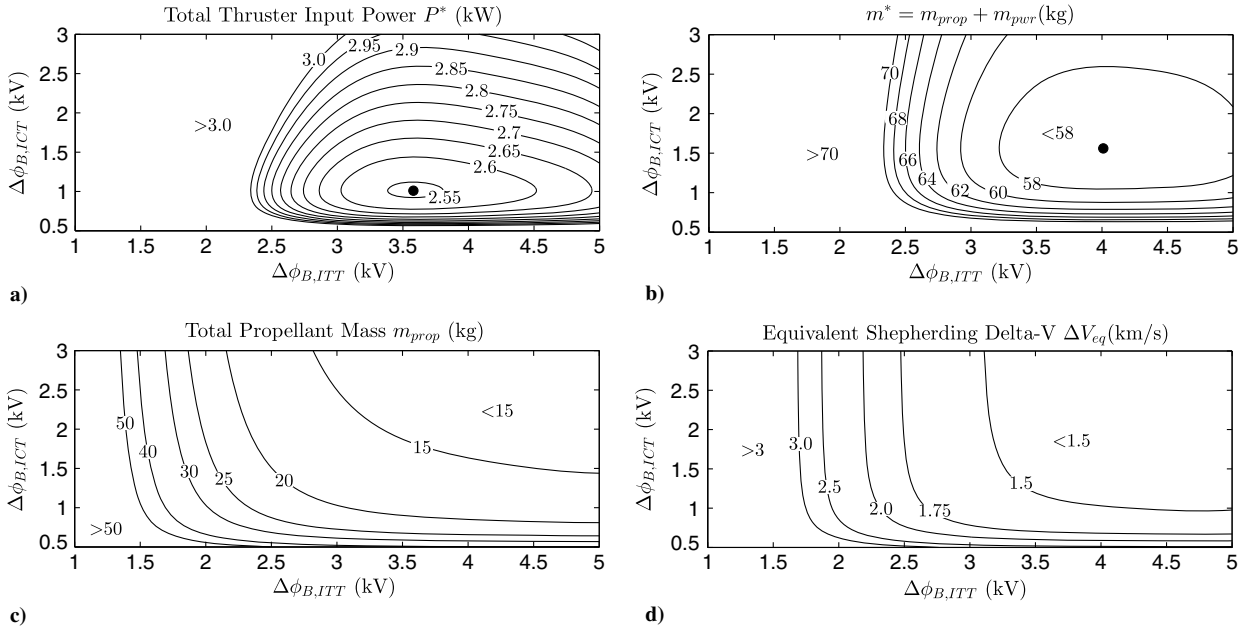

Fig. 8 Representations of a) total thrusters input power; b) optimizable EPS dedicated mass; c) total propellant mass; and d) equivalent shepherding delta-V.

the ITT voltage around this optimal point produce no significant variation in the total thruster power.

Figure 8b shows the optimizable EPS dedicated mass m^*. The optimal point now shifts to higher voltages for both the ITT and the ICT with respect to that of Fig. 8a because the total propellant mass decreases for increasing voltages. The optimal voltages (corresponding to a total mass of 56.6 kg) are (4.01, 1.56) kV. At this point, $F_{\mathrm{ITT}} = 30.5$ mN and $F_{\mathrm{ICT}} = 40.1$ mN. Observe that, for a wide region around the optimal point, variations in both the ITT and ICT voltage produce no significant changes in m^*. Moreover, the total mass savings that an optimized design yields is quite small (10–15 kg) when compared to the total expected IBS mass (500 kg).

Figure 8c shows the total propellant mass of the shepherding phase as a function of both the ITT and the ICT beam voltages. Clearly, the higher these voltages, the lower the overall propellant mass. However, the propellant mass savings of an optimized design are, again, quite small. For example, at $\Delta\phi_B = 3.5$ kV, increasing the ICT voltage from 1 to 2 kV only yields a mass savings of 5 kg.

Finally, Fig. 8d shows the equivalent shepherding delta-V ΔV_{eq}. As expected, for an ICT voltage above 1–1.5 kV, the delta-V depends essentially on the momentum transfer efficiency, and hence on the ITT voltage alone: the higher the ITT voltage, the lower the ΔV_{eq}. At low ICT voltages, however, the divergence losses of the ICT become important, and this means that the ICT mass flow necessary to achieve the required thrust increases as the voltage decreases. For this reason, the equivalent shepherding delta-V increases substantially as the ICT voltage becomes smaller. It is also pointed out that ΔV_{eq} does not represent the inertial velocity change of either the target or the IBS (shown in Table 1) but rather the propulsion delta-V of a thruster, which is equivalent (in terms of mass consumption) to the ITT–ICT system.

The main conclusion that can be extracted from the presented results is that the optimal points for the ICT and ITT beam voltages are very different. The need to guarantee a sufficiently high momentum transfer efficiency drives the optimal ITT voltage to higher values. For the ICT, on the other hand, as long as the thruster efficiency is not strongly affected, a lower voltage allows us to keep the required power low, at the expense of a higher propellant consumption. This results into an ICT optimal beam voltage, which is generally quite lower than that of the ITT.

The optimal design choice may be either based on the total dedicated mass or on the total thruster power, depending on the specific mission constraints. For example, for missions featuring a well-defined limit for the total platform power, minimization of the total thruster power should be pursued (Fig. 8a). For other missions not featuring such a stringent constraint, the total dedicated mass would represent a more adequate figure of merit for the overall electric propulsion subsystem (Fig. 8b). Nonetheless, as seen in this analysis for a single deorbiting mission, m^* is quite small with respect to the total IBS wet mass (10%); therefore, the dedicated mass optimization has only a small impact on the total mass budget.

VII. Conclusions

This paper presented a dedicated study of the optimization of the electric propulsion subsystem of an ion beam shepherd mission, which is a novel technique for contactless debris deorbiting/relocation that requires two electric thrusters: an impulse transfer thruster and an impulse compensation thruster. The optimal operational points of the impulse transfer thruster (IIT) alone and of the two thrusters considered simultaneously, expressed in terms of their beam voltages, have been identified and the corresponding optimization method described.

Dedicated design performance models [13] have been used to model the effects of changes in the operational conditions of both thrusters (beam voltage and thrust) on their performance figures.

Then, simplified plasma plume and target interaction models have been used to characterize numerically the momentum transfer efficiency, and it has been found that, for the given mission scenario, the plume physics clearly affects the design choice. First of all, the thruster must guarantee a small initial divergence angle, as the conical beam expansion is the major factor that reduces the momentum transfer to the target, and hence the efficiency of the IBS technique. Second, a high operational voltage also reduces the increase of the beam divergence due to electron thermal effects.

From the point of view of the ITT alone, it is found that an optimal beam voltage exists that maximizes the transmitted force-to-power ratio or, equivalently, that minimizes the required power for a given force on the target.

The optimization study for the whole electric propulsion subsystem has permitted identification of the optimal operational points of both thrusters simultaneously, finding that the minimum total dedicated mass or power are minimized for two different beam voltages of ITT and impulse compensation thruster (ICT), with that of the ITT much higher. The choice on whether to minimize the total dedicated mass or the total thruster power depends on the individual mission specifications.

The study presented in this paper can be further refined in the future by introducing additional effects in the total electric propulsion subsystem mass budget, such as the influence of the mass of the thruster units and of the dedicated power processing units.

In addition, although both thrusters have been considered of the same type (radio-frequency ion thrusters) to reduce the system complexity, using a different technology for the ICT, like a Hall Effect thruster, is also envisaged and should be further investigated. In fact, such thrusters generally feature a better thrust-to-power ratio than ion thrusters, thus resulting as very promising for missions with stringent constraints on the available platform power.

An important study to be addressed in future work is also the optimization of a multiple debris removal mission. In fact, the ion beam shepherd spacecraft is clearly reusable, which is a characteristic that makes it particularly appealing when compared to other active debris removal techniques. Such an optimization should take into account the time required by the rendezvous phases with each of the successive debris objects, as well as the corresponding delta-V. For what concerns the latter, its value is fixed by the mission orbital parameters and, apart from driving upwards the S/C wet mass, it only affects the mass optimization, favoring a higher specific impulse for the rendezvous thruster (ITT or ICT). On the other hand, the rendezvous phases duration affects both the mass and power optimizations, because it determines, together with the number and mass of the debris objects, the minimum force to be transmitted to the debris, for a given mission duration.

Finally, future work should also address the effects of an offcenter plume impact on the debris, which consists of a momentum transfer efficiency loss but also in an induced angular acceleration of the debris object. Recent research [4], suggested the use of a dedicated control strategy, even though the associated fragmentation risk is estimated to be quite small.

Acknowledgments

The research leading to the results of this paper was carried out within the LEOSWEEP project and received funding from the European Union Seventh Framework Programme (FP7/2007-2013) under grant agreement number 607457. Additional funding was received by Spain's Research and Development National Plan, grant ESP2013-41052

References

[1] Liou, J. C., and Johnson, N. L., "A Sensitivity Study of the Effectiveness of Active Debris Removal in LEO," *Acta Astronautica*, Vol. 64, Nos. 2–3, 2009, pp. 236–243. doi:10.1016/j.actaastro.2008.07.009

[2] Liou, J. C., Johnson, N. L., and Hill, N. M., "Controlling the Growth of Future LEO Debris Populations with Active Debris Removal," *Acta Astronautica*, Vol. 66, Nos. 5–6, 2010, pp. 648–653. doi:10.1016/j.actaastro.2009.08.005

[3] Jasper, L., Andersony, P., Schaubz, H., and McKnight, D., "Economic and Risk Challenges of Operating in the Current Space Debris Environment," *3rd European Workshop on Space Debris Modeling and Remediation*, Centre National d'Etudes Spatiales Paper 8.2, Paris, France, 2014.

[4] Bombardelli, C., and Peláez, J., "Ion Beam Shepherd for Contactless Space Debris Removal," *Journal of Guidance, Control, and Dynamics*,

Vol. 34, No. 3, May 2011, pp. 916–920.
doi:10.2514/1.51832

[5] Bombardelli, C., Urrutxua, H., Merino, M., Ahedo, E., and Peláez, J., "The Ion Beam Shepherd: A New Concept for Asteroid Deflection," *Acta Astronautica*, Vol. 90, No. 1, 2013, pp. 98–102.
doi:10.1016/j.actaastro.2012.10.019

[6] Merino, M., Ahedo, E., Bombardelli, C., Urrutxua, H., and Peláez, J., "Ion Beam Shepherd Satellite for Space Debris Removal," *Progress in Propulsion Physics*, Vol. 4, EUCASS Advances in Aerospace Sciences, edited by DeLuca, L. T., Bonnal, C., Haidn, O. J., and Frolov, S. M., Torus Press, Moscow, 2013, pp. 789–802, Chap. 8.
doi:10.1051/eucass/201304789

[7] Ruiz, M., Urdampilleta, I., Bombardelli, C., Ahedo, E., Merino, M., and Cichocki, F., "The FP7 LEOSWEEP Project: Improving Low Earth Orbit security with Enhanced Electric Propulsion," *Space Propulsion 2014*, 3AF Paper 2980908, Paris, France, 2014.

[8] Cichocki, F., Merino, M., and Ahedo, E., "Modeling and Simulation of EP Plasma Plume Expansion into Vacuum," *50th AIAA/ASME/SAE/ASEE Joint Propulsion Conference*, AIAA Paper 2014-3828, 2014.

[9] Merino, M., Cichocki, F., and Ahedo, E., "Collisionless Plasma Thruster Plume Expansion Model," *Plasma Sources Science and Technology*, Vol. 24, No. 3, 2015, Paper 035006.
doi:10.1088/0963-0252/24/3/035006

[10] Bombardelli, C., Urrutxua, H., Merino, M., Ahedo, E., and Peláez, J., "Relative Dynamics and Control of an Ion Beam Shepherd Satellite," *Spaceflight Mechanics 2012*, Vol. 143, Advances in the Astronautical Sciences, edited by McAdams, J. V., McKinley, D. P., Berry, M. M., and Jenkins, K. L., Univelt, Escondido, CA, 2012, pp. 2145–2158.

[11] Cichocki, F., Merino, M., Ahedo, E., Feili, D., and Ruiz, M., "Electric Propulsion Subsystem Optimization for Ion Beam Shepherd Missions," *34th International Electric Propulsion Conference and 6th Nano-Satellite Symposium*, Electric Rocket Propulsion Soc. Paper 2015-35, Fairview Park, OH, 2015.

[12] Goebel, D. M., and Katz, I., *Fundamentals of Electric Propulsion: Ion and Hall Thrusters*, JPL Space Science and Technology Series, Pasadena, CA, 2008, pp. 243–324.

[13] Feili, D., Ruiz, M., Merino, M., Cichocki, F., Ahedo, E., Smirnova, M., and Dobkevicius, M., "Impulse Transfer Thruster for an Ion Beam Shepherd Mission," *34th International Electric Propulsion Conference*, IEPC Paper 2015-382, Electric Rocket Propulsion Soc. (ERPS), Fairview Park, OH, 2015.

[14] Beal, B. E., Gallimore, A., Haas, J. M., and Hargus, W. A., "Plasma Properties in the Plume of a Hall Thruster Cluster," *Journal of Propulsion and Power*, Vol. 20, No. 20, pp. 985–991, 2004.

[15] Boyd, I. D., and Yim, J. T., "Modeling of the Near Field Plume of a Hall Thruster," *Journal of Applied Physics*, Vol. 95, No. 9, April 2004, Paper 4575.
doi:10.1063/1.1688444

[16] Foster, J. E., Soulas, G. C., and Patterson, M. J., "Plume and Discharge Plasma Measurements of an NSTAR-Type Ion Thruster," *36th Joint Propulsion Conference and Exhibit*, AIAA Paper 2000-3812, 2000.

[17] Dannenmayer, K., Mazouffre, S., Ahedo, E., and Merino, M., "Hall Effect Thruster Plasma Plume Characterization with Probe Measurements and Self-Similar Fluid Models," *48th AIAA/ASME/SAE/ASEE Joint Propulsion Conference & Exhibit*, AIAA Paper 2012-4117, 2012.

[18] Azziz, Y., "Experimental and Theoretical Characterization of a Hall Thruster Plume," Ph.D. Dissertation, Massachusetts Inst. of Technology, Cambridge, MA, 2007.

[19] Parks, D. E., and Katz, I., "A Preliminary Model of Ion Beam Neutralization," *14th International Electric Propulsion Conference*, Electric Rocket Propulsion Soc. Paper 79-2049, Fairview Park, OH, 1979.

[20] Anderson, J. R., Goodfellow, K. D., Polk, J. E., Rawlin, V. K., Sovey, J. S., and Patterson, M. J., "Performance Characteristics of the NSTAR Ion Thruster During an On-Going Long Duration Ground Test," *IEEE Aerospace Conference Proceedings*, Vol. 4, IEEE, Piscataway, NJ, 2000, pp. 99–122.

[21] Soulas, G. C., "Improving the Total Impulse Capability of the NSTAR Ion Thruster with Thick-Accelerator-Grid Ion Optics," *27th International Electric Propulsion Conference*, Electric Rocket Propulsion Soc. Paper 2001-081, Fairview Park, OH, Oct. 2001.

L. King
Associate Editor